


**Anharmonicity-induced strong temperature-dependent thermal conductivity in  $\text{CuInX}_2$  ( $X=\text{Se, Te}$ )**Yongheng Li , Junyan Liu, and Jiawang Hong <sup>\*</sup>*School of Aerospace Engineering, Beijing Institute of Technology, Beijing 100081, China* (Received 16 July 2022; revised 3 September 2022; accepted 14 September 2022; published 29 September 2022)

The lattice thermal conductivity ( $\kappa_L$ ) of most single crystals usually follows  $T^{-1}$  temperature dependent relation at high temperature region. Here, we investigate the microscopic mechanism of the significant deviation of  $\kappa_L \sim T^{-1}$  rule in Cu-based chalcopyrite compounds  $\text{CuInX}_2$  ( $X=\text{Se, Te}$ ) by performing first-principles calculations and solving Peierls-Boltzmann transport equation with phonon anharmonic renormalization. The temperature sensitive second-order force constants lead to the dramatically softened optical phonon bands, which contributes to the enlarged phonon scattering phase space and consequent enhanced scattering rate. The strong temperature dependent thermal conductivity in  $\text{CuInX}_2$  ( $X=\text{Se, Te}$ ) can be well reproduced when calculating thermal conductivity with renormalization force constants. The motion of Cu contributes the most to the large anharmonicity at high temperature, which makes the anharmonic renormalization non-negligible for estimating accurate lattice dynamic and thermal conductivity. Our work will deepen the understanding of thermal transport property of Cu-based chalcopyrite, which is helpful for designing better thermoelectric or photovoltaic devices.

DOI: [10.1103/PhysRevB.106.094317](https://doi.org/10.1103/PhysRevB.106.094317)**I. INTRODUCTION**

Thermal conductivity is an important property for thermoelectrics [1,2], photovoltaics [3,4], and thermal barrier coatings [5]. The conversion efficiency of thermoelectrics can be described with a dimensionless figure of merit  $zT$ , where  $zT = \sigma^2 S \kappa^{-1} T$  [6]. The  $S$  indicates the Seebeck coefficient,  $\sigma$  is electrical conductivity,  $\kappa$  is thermal conductivity, and  $T$  is temperature. The material with the lower thermal conductivity contributes to the larger  $zT$  and accompanying the better thermoelectric performance. Besides, the lifetime and performance of photovoltaics are closely related to the temperature gradient in devices, which emphasizes the significance of thermal transport properties [7,8].

The Cu-based diamondlike chalcopyrite compounds are not only good thermoelectric material candidates, such as  $\text{CuInTe}_2$  and  $\text{CuGaTe}_2$  [9–11], but also great photovoltaics candidates, such as  $\text{CuInSe}_2$ , etc [12–14]. To optimize the performance of Cu-based diamondlike chalcopyrite compounds, the modulation of thermal conductivity  $\kappa$  is an effective way based on classic Peierls-Boltzmann transport equation (PBTE), especially in lifting thermoelectric performance by nanostructure engineering, alloying, etc [15–17]. The three-phonon scattering theory is an efficient way to solve the PBTE at nanoscale, which predicts the  $\kappa_L \sim T^{-1}$  relation at high temperature due to the population of scattering phonons [18–20]. Though various ways have been proposed to tune the thermal transport property of Cu-based diamondlike chalcopyrite compounds by controlling the phonon scattering process [21–23], there is still a long-time puzzling phenomenon: the significant deviation of  $\kappa_L \sim T^{-1}$  relation,

especially in  $\text{CuInSe}_2$  and  $\text{CuInTe}_2$  [24–26], which indicates the failure of three-phonon scattering theory.

The materials with the deviation of the  $\kappa_L \sim T^{-1}$  rule has attracted intensive attention recently and different theories are proposed to explain this unusual thermal transport properties. The weak temperature dependent thermal conductivity in single crystals with low or ultralow thermal conductivity are observed and explained. For example, the quartic anharmonicity of rattlers result in the glasslike thermal conductivity in complex crystal  $\text{Ba}_8\text{Ga}_{16}\text{Ge}_{30}$  [27]. The coherent phonon interaction contributes to the weak temperature dependence of thermal conductivity in  $\text{CsPbBr}_3$  and  $\text{BaSnS}_2$  [28,29]. To calculate more accurate thermal conductivity of  $\text{TlInTe}_2$  and  $\text{Tl}_3\text{VSe}_4$  at finite temperature, the self-consistent phonon theory and high order phonon interaction should be taken into consideration [30,31]. The temperature dependent force constants explain well for the glasslike thermal conductivity of  $\text{Mg}_3\text{Sb}_2$  and  $\text{Cs}_2\text{AgBiBr}_6$  [32,33]. Also, the two channel model is an effective way to correct the prediction of thermal conductivity [34]. Besides the weak temperature dependence, there is also strong temperature dependent thermal conductivity in single crystals, such as  $\text{CuInSe}_2$  and  $\text{CuInTe}_2$  [24–26]. The strong four phonon interaction usually accounts for the strong temperature dependent thermal conductivity, which has been well confirmed in BAs, BN, etc. [35–37]. Understanding these different mechanisms can introduce more factors to control phonon scattering and finally effectively regulate the thermal conductivity [38]. However, there are few systematic studies on strong temperature dependence of thermal conductivity in Cu-based diamondlike chalcopyrite compounds, except for  $\text{CuInTe}_2$  which has been considered as the material with strong four phonon interaction [39].

Here, we propose that the strong temperature dependent thermal conductivity of  $\text{CuInX}_2$  ( $X=\text{Se, Te}$ ) can be well described with the anharmonic renormalization by conducting

<sup>\*</sup>Corresponding author: hongjiw@bit.edu.cn

the first-principles calculations based on the density functional theory (DFT) without invoking four phonon interaction. We show that the large anharmonicity at high temperature leads to the optical phonon bands softening dramatically in  $\text{CuInX}_2$  ( $X=\text{Se}, \text{Te}$ ). The scattering rate considering the anharmonic renormalization in  $\text{CuInX}_2$  are obviously enhanced compared with those calculations only with force constants at 300 K, which is closely related to the temperature sensitive second-order force constants (FC2) inducing the enlarged phonon scattering phase space. It is found that the temperature sensitive motion of Cu contributes to large anharmonicity at high temperature, making the anharmonic renormalization non-negligible for predicting accurate temperature dependent lattice dynamic and thermal conductivity of  $\text{CuInX}_2$  ( $X=\text{Se}, \text{Te}$ ). This work can deepen our understanding of the thermal transport properties of these Cu-based compounds to design better thermometric or photovoltaic devices.

## II. METHOD

The initial conventional structures with 4 Cu atoms, 4 In atoms and 8 X ( $X=\text{Se}, \text{Te}$ ) atoms were relaxed with the Vienna *ab initio* simulation package (VASP) [43]. The local density approximation (LDA) can describe the lattice constant much better than the generalized gradient approximation (GGA) and thus we employed the LDA for all calculation in this paper, as shown in Note 1 and Table 1 in the Supplemental Material [44,45]. The kinetic energy cutoff was set as 600 eV and the electronic energy tolerance was set to  $10^{-6}$  eV. The force on each atom was set to be smaller than  $0.001 \text{ eV}/\text{\AA}$ . The converged  $8 \times 8 \times 2$  Monkhorst-Pack K-point [46] was used to sample the Brillouin zone. We added the temperature dependent thermal expansion from experiment results [47,48] to the full relaxed  $\text{CuInX}_2$  ( $X=\text{Se}, \text{Te}$ ) structures based on DFT calculation, which were then used as the initial structure for quasiharmonic approximation calculation and molecular dynamic calculations at each temperature. Then we add thermal expansion, the thermal expansion related parameters, and the lattice constants. The results after adding thermal expansion are shown in Note 2, Table 2, and Table 3 in the Supplemental Material, respectively [44]. The phonon dispersion with quasiharmonic approximation were calculated with the finite displacement method with Phonopy [49]. The  $2 \times 2 \times 1$  supercells and the  $4 \times 4 \times 2$  Monkhorst-Pack [46] K-point were used for both  $\text{CuInSe}_2$  and  $\text{CuInTe}_2$ .

To consider the phonon anharmonic renormalization, we introduced the temperature dependent effective potential (TDEP) method here [50–52], which can well describe the anharmonic characteristic in material systems, especially at high temperature. The *ab initio* molecular dynamics (AIMD) calculation was performed in nondiagonal  $[[3,0,2],[0,3,1],[1,1,4]]$  supercell (216 atoms) within a canonical ensemble using a Nosé-Hoover thermostat, which provided force and displacement for extracting force constants (FCs) in TDEP. These supercells are based on primitive cell of  $\text{CuInX}_2$  ( $X=\text{Se}, \text{Te}$ ). The nondiagonal dimension is adopted in order to configure the cubiclike supercell, which can effectively reduce the computational cost of acquiring converged phonon dispersions [53]. A plane-wave cutoff of 450 eV was used in all the AIMD calculations. The K-point was set as  $\Gamma$  only. Around

a total number of 3ps with 2 fs/step for each temperature in  $\text{CuInX}_2$  ( $X=\text{Se}, \text{Te}$ ) were calculated. The cutoff radii of second order force constants are set as  $10 \text{ \AA}$  for both  $\text{CuInSe}_2$  and  $\text{CuInTe}_2$ . The cutoff radii of third order force constants are set as  $6.6 \text{ \AA}$  for  $\text{CuInSe}_2$  and  $7.3 \text{ \AA}$  for  $\text{CuInTe}_2$ , respectively. We transformed the TDEP format FC to the ShengBTE format FC with the help of Hiphive and our own code [54,55]. And then we calculated thermal conductivity with ShengBTE because ShengBTE can be more convenient to analyze phonon scattering rate, etc. [18]. The converged q-space grid  $13 \times 13 \times 13$  was applied to calculate the thermal conductivity. More related convergence tests can be found in Note 3 and Figs. S1–S4 in the Supplemental Material [44].

## III. RESULTS AND DISCUSSION

Figures 1(a) and 1(d) show the temperature dependent phonon dispersion of  $\text{CuInSe}_2$  and  $\text{CuInTe}_2$ , respectively. Our calculations at 300 K of the two materials are in good agreement with available Raman experiment result [40–42]. The details of comparison between the calculation and Raman experiments at 300 K can be found in Table 4 in the Supplemental Material [44]. In  $\text{CuInSe}_2$  and  $\text{CuInTe}_2$ , the optical phonon bands obviously soften when temperature increases from 300 K to high temperature, especially for high energy bands. The softened optical modes with increasing temperature in  $\text{CuInTe}_2$  has been confirmed by recent Raman experiment [39]. The obvious softened optical phonon bands at high temperature indicate the significant change of FC2 after considering the anharmonic renormalization. Compared with dramatically softened optical phonon bands, the change of acoustic phonon bands is much smaller, which may bring little change of group velocity to affect the thermal conductivity. Figures 1(b), 1(c), 1(e), and 1(f) are phonon density of states (DOS) for  $\text{CuInSe}_2$  and  $\text{CuInTe}_2$ , respectively. As shown in Figs. 1(b) and 1(c), the phonon peaks decrease to the lower energy with temperature increasing, corresponding to the softened optical phonon bands for  $\text{CuInSe}_2$  at high temperature. Besides, there is a pseudo band gap around 10 meV (indicated by two dashed black lines), which decreases from 3.5 meV at 300 K to 1.9 meV at 750 K. Below the pseudogap, the broad gray peak narrows down obviously as black arrows point to, which indicates the phonon bandwidth becomes much smaller when temperature increases from 300 to 750 K. The peaks of the projected density of states (DOS) of Cu, In and X ( $X=\text{Se}, \text{Te}$ ) in low energy region become much sharper when temperature increases from 300 to 750 K, as shown in circled with dashed lines, especially for Cu. There are also similar changes in phonon DOS of  $\text{CuInTe}_2$ , as shown in Figs. 1(e) and 1(f). These changes in low energy region with temperature increasing will effectively introduce more phonon scattering channels to decrease thermal conductivity, which will be discussed later.

To confirm the importance of considering anharmonicity in calculation, we also calculated the phonon dispersion of  $\text{CuInSe}_2$  and  $\text{CuInTe}_2$  with quasiharmonic approximation, as shown in Figs. 2(a) and 2(d). The results from quasiharmonic approximation shows that the low energy optical phonon nearly unchanged when temperature increases, which is contrary to the previous Raman experiments on  $\text{CuInTe}_2$

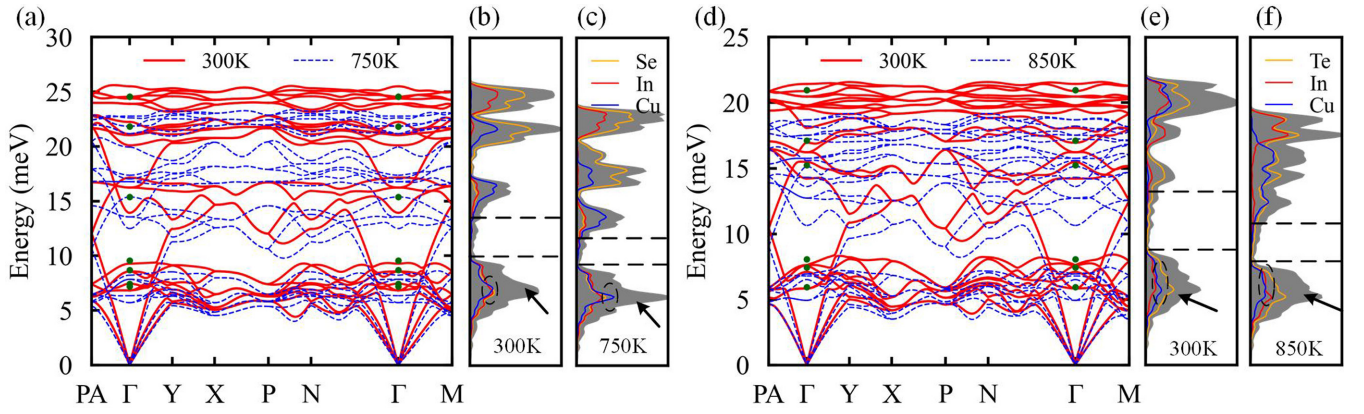


FIG. 1. (a) and (d) are phonon dispersion of  $\text{CuInSe}_2$  and  $\text{CuInTe}_2$ , respectively. The dark green points are Raman experiment results at 300 K [40–42]. The gray shade regions in (b), (c) and (e), (f) represent total phonon density of states (DOS) for  $\text{CuInSe}_2$  and  $\text{CuInTe}_2$  at 300 K and high temperature (750 K for  $\text{CuInSe}_2$  and 850 K for  $\text{CuInTe}_2$ ), respectively. The DOS projected on Cu, In, and X ( $X=\text{Se}, \text{Te}$ ) atoms are shown with blue, red, and orange solid lines, respectively. The black dashed lines indicate the pseudoband gap around 10 meV.

[39]. As shown in Figs. 2(b) and 2(e), the phonon dispersion with anharmonic renormalization at 300 K seems to be softer than those with quasiharmonic approximation. Compared with Raman experiment at 300 K, the phonon dispersion of  $\text{CuInSe}_2$  and  $\text{CuInTe}_2$  with anharmonic renormalization show better agreement than those with quasiharmonic approximation [40–42]. When temperature increases, the differences of phonon dispersion calculated by two methods become much more distinct, as shown in Figs. 2(c) and 2(f). In all, the anharmonicity plays a critical role to describe much better

temperature dependent lattice dynamic of  $\text{CuInX}_2$  ( $X=\text{Se}, \text{Te}$ ), which will help to calculate the accurate temperature dependent thermal conductivity.

Then, we calculated the temperature dependent thermal conductivity of  $\text{CuInX}_2$  ( $X=\text{Se}, \text{Te}$ ) along the [100] direction, as shown in Figs. 3(a) and 3(b). The calculation of  $\text{CuInSe}_2$  with only FC at 300K, which brings the  $\kappa \sim T^{-1}$  relation, shows obvious deviation from experiment results ( $\kappa \sim T^{-1.6}$ ) [57]. However, when considering the temperature dependent FC, the calculation result shows  $\kappa \sim T^{-1.8}$

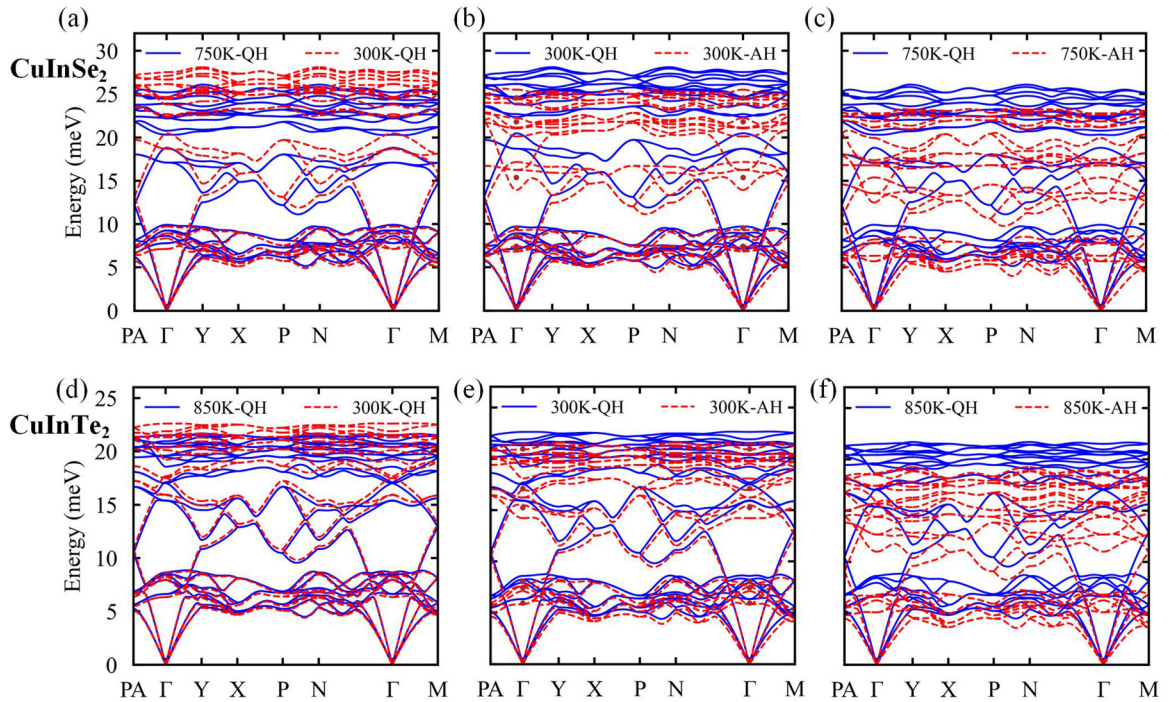


FIG. 2. (a)–(c) and (d)–(f) are calculated phonon dispersion of  $\text{CuInSe}_2$  and  $\text{CuInTe}_2$  with quasiharmonic (QH) approximation and anharmonic (AH) renormalization, respectively. In (a) and (d), the red lines indicate calculation at 300 K and the blue lines indicate calculation at high temperature (750 K for  $\text{CuInSe}_2$  and 850 K for  $\text{CuInTe}_2$ ). In (b), (c) and (e), (f), the red lines indicate calculation considering anharmonicity and the blue lines indicate the calculation with QH. The brown points in (b) and (e) are Raman experiment results at 300 K [40–42].

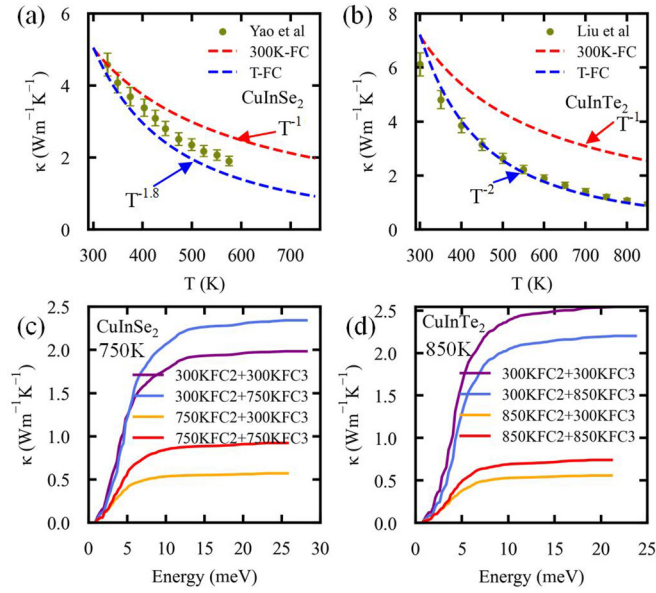


FIG. 3. (a) and (b) are temperature dependent thermal conductivity along [100] direction of  $\text{CuInSe}_2$  and  $\text{CuInTe}_2$ , respectively. The red lines are calculated with the force constant at 300 K and the blue lines are calculated with the temperature dependent force constants. The points are measured thermal conductivity [56,57]. (c) and (d) are energy dependent thermal conductivity along [100] direction of  $\text{CuInSe}_2$  and  $\text{CuInTe}_2$  at high temperature (750 K for  $\text{CuInSe}_2$  and 850 K for  $\text{CuInTe}_2$ ), respectively. The purple, royal blue, orange, and red lines represent the thermal conductivity calculated with both FC2 and FC3 at 300 K, FC2 at 300 K and FC3 at high temperature, FC2 at high temperature and FC3 at 300 K, both FC2 and FC3 at high temperature, respectively.

relation, which agrees much better with experiment results. The  $\text{CuInTe}_2$  has a similar situation. After considering the temperature dependent FC, the calculation result changes from  $\kappa \sim T^{-1}$  to  $\kappa \sim T^{-2}$ , which matches better with experiment result  $\kappa \sim T^{-1.7}$  [56].

Figures 3(c) and 3(d) help us to understand how temperature dependent FC contributes to this strong temperature dependent thermal conductivity in  $\text{CuInX}_2$  ( $X=\text{Se}, \text{Te}$ ). As shown in Fig. 3(c), the energy dependent thermal conductivity of  $\text{CuInSe}_2$  at 750 K shows the phonons below  $\sim 13$  meV contribute to the most thermal transport. We firstly use the second-order force constant at 300 K (300 K-FC2) and the third-order force constant at 300 K (300 K-FC3) to calculate the thermal conductivity at 750 K for  $\text{CuInSe}_2$ , which generates  $\kappa_L=1.81$  W/mK. When changing from 300 K-FC2 to 750 K-FC2 but remaining 300 K-FC3, the thermal conductivity decreases significantly from 1.81 to 0.57 W/mK, suggesting the critical role of the temperature dependent FC2 on the thermal conductivity at high temperature. Then, we use 750 K-FC2 and 750 K-FC3 to calculate the thermal conductivity to obtain the thermal conductivity of 0.92 W/mK. Figure 3(d) indicates that the  $\text{CuInTe}_2$  also shows similar changes of thermal conductivity when using different force constants as done with  $\text{CuInSe}_2$ . It's worth noting that when changing from 300 K-FC2 to 850 K-FC2 and keeping 300 K-FC3, the thermal conductivity of  $\text{CuInTe}_2$  decreases from 2.45

W/mK to 0.56 W/mK, about a fivefold decrease. After using the both FC2 and FC3 at 850K, the discrepancy of thermal conductivity of  $\text{CuInTe}_2$  between the calculation and experiment decreases from 170% to 18% [56]. We also calculate thermal conductivity with 300 K-FC2 and 750 K-FC3(850 K-FC3) for  $\text{CuInSe}_2$ ( $\text{CuInTe}_2$ ), where the thermal conductivity of  $\text{CuInSe}_2$ ( $\text{CuInTe}_2$ ) only changes 17.97%(11.81%) compared with those using 300 K-FC2 and 300 K-FC3. It is obvious that leaving 300 K-FC2 and changing from 300 K-FC3 to high temperature FC3 has much smaller influence on thermal conductivity than those changing from 300 K-FC2 to high temperature FC2 and leaving 300 K-FC3. The huge differences on thermal conductivity when only changing from 300 K-FC2 to that at high temperature(750 K for  $\text{CuInSe}_2$  and 850 K for  $\text{CuInTe}_2$ ) indicates that the thermal conductivity is significantly sensitive to the accurate FC2. It also reflects that the critical role of phonon anharmonicity in describing lattice dynamic and thermal conductivity of these two material systems as mentioned before.

Next, we will discuss why the anharmonic renormalization FC2 is crucial to calculate much better thermal conductivity at high temperature in details. As is well known, the thermal conductivity can be described as  $\kappa_L = (1/3)Cv^2\tau$ , where the  $C$ ,  $v$ , and  $\tau$  indicate the heat capacity, group velocity and phonon lifetime, respectively. The heat capacity  $C$  of the same material almost keeps constant at high temperature, so we then focus on the group velocity and phonon lifetime. Figures 4(a) and 4(d) show the extracted temperature dependent group velocity for  $\text{CuInSe}_2$  and  $\text{CuInTe}_2$ , respectively. The group velocity of transversal acoustic (TA) phonon bands along  $\Gamma - \text{M}$  seem to show little change with temperature in two materials. The group velocity of longitudinal acoustic (LA) phonon bands show slight drop for the two materials,  $\sim 11.53\%$  for  $\text{CuInSe}_2$  and  $\sim 8.97\%$  for  $\text{CuInTe}_2$ . Figure S5 shows that the group velocity along  $\Gamma - \text{Y}$  has similar changes to those along  $\Gamma - \text{M}$ . These little changes of group velocity are consistent with the small changes of acoustic phonon bands as shown in Figs. 1(a) and 1(d). The slight drop of group velocity of LAs in  $\text{CuInX}_2$  ( $X=\text{Se}, \text{Te}$ ) will reduce the thermal conductivity, but it is still difficult to describe the reduction in thermal conductivity by more than a factor of two after considering the temperature dependent force constants, as shown in Figs. 3(c) and 3(d).

After excluding the effect of group velocity, the decrease of thermal conductivity after utilizing temperature dependent force constants must be related to the phonon lifetime  $\tau$ . As shown in Figs. 4(b) and 4(e), the phonon scattering rate  $\tau^{-1}$  under  $\sim 13$  meV of  $\text{CuInSe}_2$  and  $\text{CuInTe}_2$  are obviously enhanced after using temperature dependent force constants. The scattering rate can be described as [58]

$$\begin{aligned} \tau_{\mathbf{q}_s}^{-1} = & \frac{36}{\hbar^2} \sum_{\mathbf{q}_1, \mathbf{q}_2, s_1, s_2} |\Phi_{\mathbf{q}, \mathbf{q}_1, \mathbf{q}_2, s, s_1, s_2}|^2 \\ & \times \{ (n_1 + n_2 + 1) [\delta(\omega_1 + \omega_2 - \omega_{\mathbf{q}_s}) \\ & - \delta(\omega_1 + \omega_2 + \omega_{\mathbf{q}_s})] \\ & + (n_2 - n_1) [\delta(\omega_1 - \omega_1 - \omega_{\mathbf{q}_s}) \\ & - \delta(\omega_1 - \omega_2 + \omega_{\mathbf{q}_s})] \}, \end{aligned} \quad (1)$$

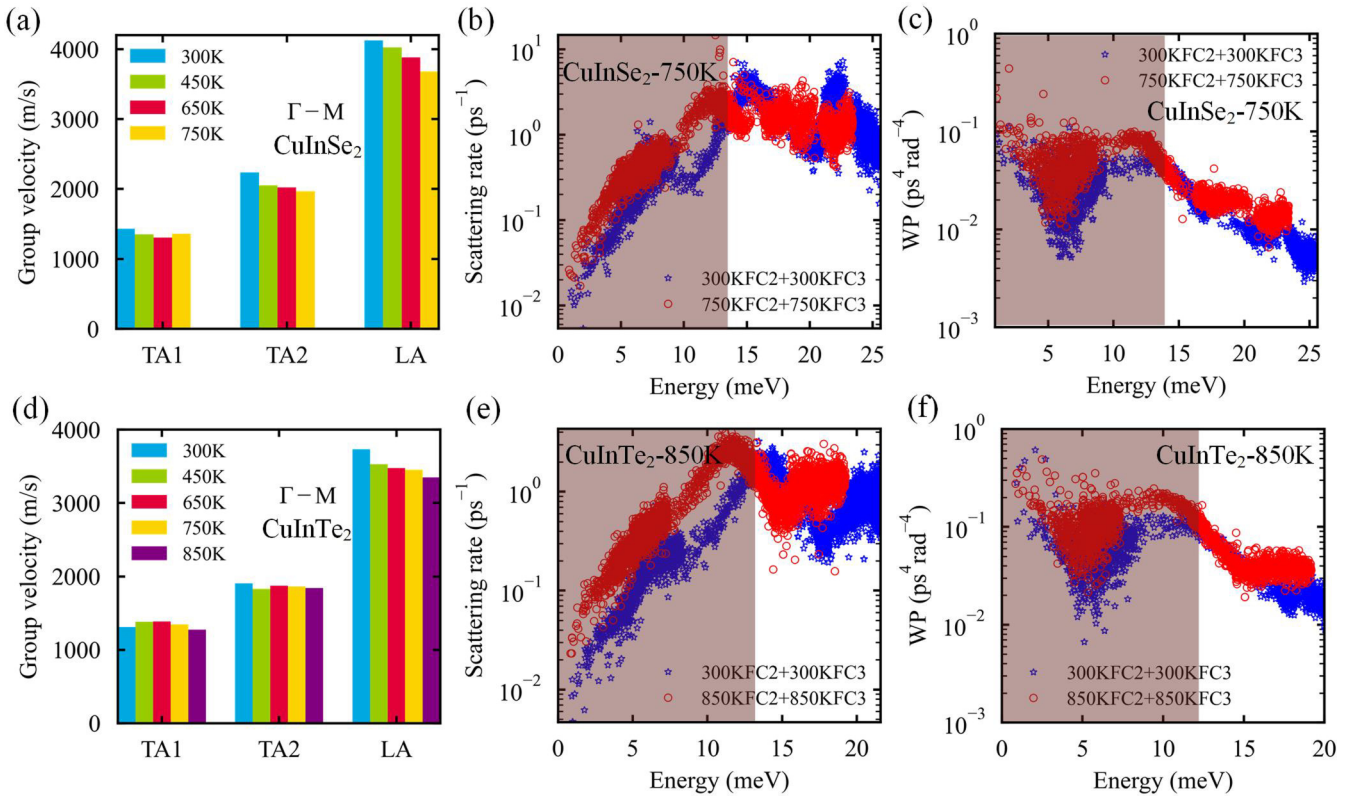


FIG. 4. (a) and (d) are group velocity of CuInSe<sub>2</sub> and CuInTe<sub>2</sub> at different temperature along  $\Gamma$ -M, respectively. The TA and LA represent transversal acoustic bands and longitudinal acoustic bands, respectively. (b) and (e) are the energy dependent scattering rate of CuInSe<sub>2</sub> and CuInTe<sub>2</sub> at high temperature, respectively. (c) and (f) are energy dependent weighted phonon scattering phase space at high temperature (750 K for CuInSe<sub>2</sub> and 850 K for CuInTe<sub>2</sub>). The blue stars and red points indicate calculation with force constants at 300 K and those at high temperature, respectively.

where the  $n_{i(i=1,2)} = (e^{\hbar\omega_{\mathbf{q}_s}/k_B T} - 1)^{-1}$  indicates the Bose occupation of phonons  $\omega_{\mathbf{q}_s}$  under specific temperature  $T$ . The  $\delta$  function is related to the phase space, which is mainly based on calculation with FC2 to guarantee the energy and momentum conservation [59]. The  $\Phi_{\mathbf{q},\mathbf{q}_1,\mathbf{q}_2,s,s_1,s_2}$  is FC3, which is related to the Grüneisen parameter [60]. So we extracted the scattering phase space and Grüneisen parameter for further studying the origin of the enhanced scattering rate in CuInX<sub>2</sub> ( $X=\text{Se, Te}$ ).

As shown in Figs. 4(c) and 4(f), the scattering phase space under  $\sim 13$  meV obviously lifts after considering anharmonic renormalization force constants in CuInSe<sub>2</sub> and CuInTe<sub>2</sub>. This energy region corresponds to where the scattering rate distinctly enhances as shown in Figs. 4(b) and 4(e), which mainly depends on the anharmonic renormalization FC2. However, the FC3 with anharmonic renormalization brings few changes in the temperature-dependent Grüneisen parameter in CuInX<sub>2</sub> ( $X=\text{Se, Te}$ ) as shown in Figs. S6. This is consistent with that the FC2 is much more sensitive to temperature and plays much a more important role in predicting accurate thermal conductivity than FC3 as mentioned before. The temperature sensitive FC2 leads to the softened optical phonon bands and then results in the smaller low energy phonon bandwidth, as well as a narrower pseudo phonon band gap as shown in Figs. 1(b), 1(c), 1(e), and 1(f). The energy region of enlarged scattering phase space corresponds to that of

changes in low energy phonon bandwidth and pseudo phonon band gap, whose energy regions are all below  $\sim 13$  meV. Therefore, it is clear that the anharmonic renormalization FC2 mainly brings large scattering phase space and then leads to an enhanced scattering rate to decrease the thermal conductivity in CuInX<sub>2</sub> ( $X=\text{Se, Te}$ ).

It is necessary to perform the anharmonic renormalization due to the strong anharmonicity at high temperature in CuInX<sub>2</sub> ( $X=\text{Se, Te}$ ). Then, we explore the origin of strong anharmonicity in CuInX<sub>2</sub> ( $X=\text{Se, Te}$ ). As shown in Figs. 5(a) and 5(d), the projected FC2 to bond direction  $\Phi_B$  of the Cu-X ( $X=\text{Se or Te}$ ) decreases much quicker than others when the temperature increases, in which the  $\Phi_B$  can be described as [61]

$$\Phi_B(i, j) = \left| \begin{pmatrix} \Phi_{i,j}^{xx} & \Phi_{i,j}^{xy} & \Phi_{i,j}^{xz} \\ \Phi_{i,j}^{yx} & \Phi_{i,j}^{yy} & \Phi_{i,j}^{yz} \\ \Phi_{i,j}^{zx} & \Phi_{i,j}^{zy} & \Phi_{i,j}^{zz} \end{pmatrix} \begin{pmatrix} \vec{r}_j - \vec{r}_i \\ |\vec{r}_j - \vec{r}_i| \end{pmatrix} \right|, \quad (2)$$

where the  $(i, j)$  indicates the different atom pairs, the  $\vec{r}_i$  and  $\vec{r}_j$  indicate atom position in the pair. The larger decrease of  $\Phi_B$  of Cu-X ( $X=\text{Se, Te}$ ) indicates the weaker interaction between Cu and X atoms at high temperature, compared with In-Se or In-Te bonds. Figures 5(b) and 5(e) show that the Cu has the largest temperature dependent mean square displacement  $U$  among all the elements. Besides, the phonon anharmonic

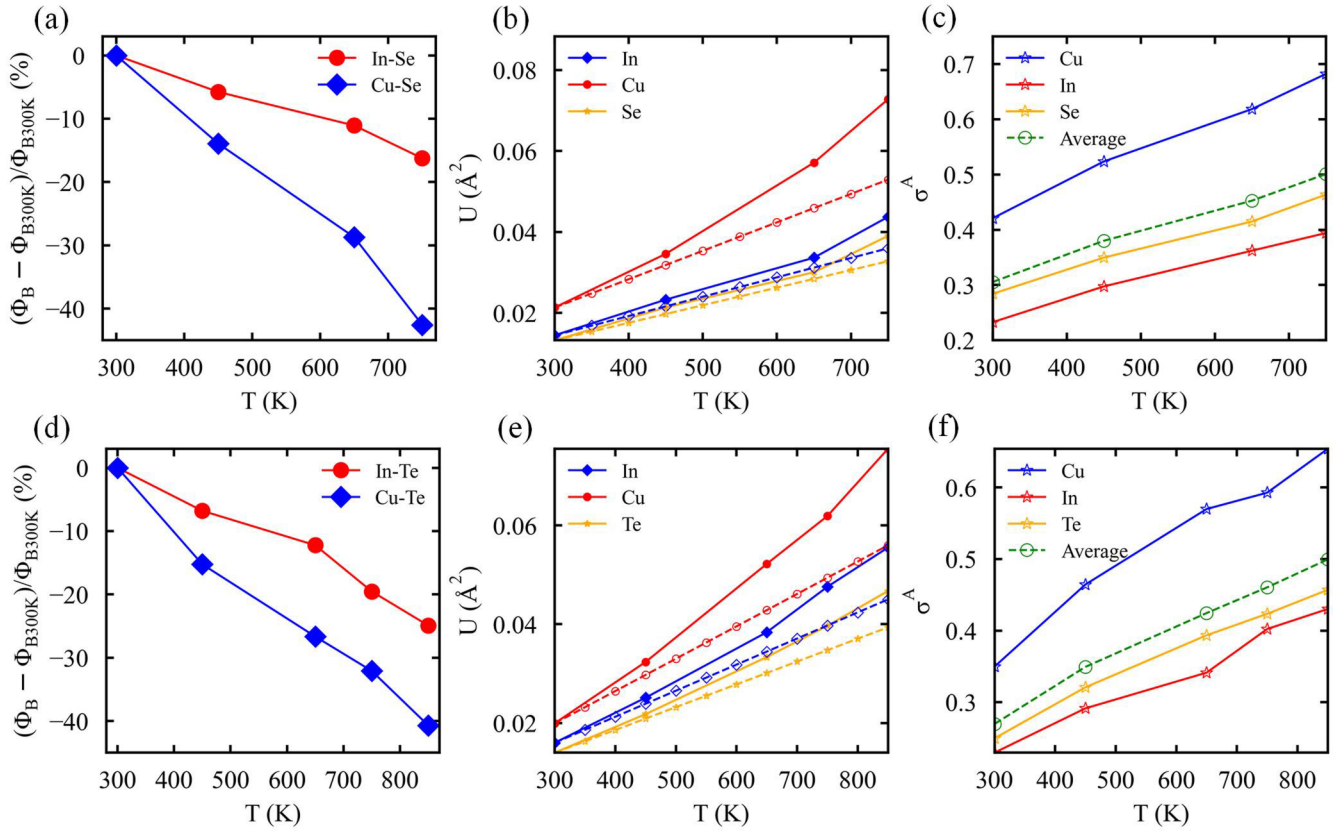


FIG. 5. (a) and (d) are temperature dependent change of the FC2 projected to the bond direction  $\Phi_B$  at 300 K for CuInSe<sub>2</sub> and CuInTe<sub>2</sub>, respectively. The blue and red lines indicate the FC2 projected to Cu-X and In-X(X=Se,Te) bond direction, respectively. (b) and (e) are temperature dependent mean square displacement  $U$  for CuInSe<sub>2</sub> and CuInTe<sub>2</sub>, respectively. The dashed lines are calculated with the FC2 at 300 K and the solid lines are calculated with the temperature dependent FC2. The blue, red, and orange lines indicate the  $U$  of In, Cu and X(X=Se, Te), respectively. (c) and (f) are temperature dependent degree of anharmonicity of atoms  $\sigma^A$ , where  $\sigma^A$  indicates the standard deviation of the distribution of anharmonic force components. The blue, red, and orange solid lines indicate the  $\sigma^A$  of Cu, In and X(X=Se, Te), respectively. The dashed lines are average  $\sigma^A$ .

renormalization bring the largest change in  $U$  of Cu, which arrives to  $\sim 47.29\%$  for CuInSe<sub>2</sub> and  $\sim 34.92\%$  for CuInTe<sub>2</sub>. To quantitatively estimate the anharmonicity of atoms in two materials, we use the standard deviation of the distribution of anharmonic force components as described [62]

$$\sigma^A(T) = \frac{\sigma[F^A]_T}{\sigma[F]_T} = \sqrt{\frac{\sum_{l,\alpha} \langle (F_{l,\alpha}^A)^2 \rangle_T}{\sum_{l,\alpha} \langle (F_{l,\alpha})^2 \rangle_T}}, \quad (3)$$

$$F_{l,\alpha}^A(\mathbf{R}) = F_{l,\alpha}(\mathbf{R}) - F_{l,\alpha}^{(2)}(\mathbf{R}), \quad (4)$$

$$F_{l,\alpha}^{(2)}(\mathbf{R}) = - \sum_{J,\beta} \Phi_{l,J}^{\alpha,\beta} \Delta R_\beta^J, \quad (5)$$

where the  $F_{l,\alpha}$  are real force components (can be extracted directly from AIMD) in material system,  $F_{l,\alpha}^{(2)}$  are force components from harmonic model and  $F_{l,\alpha}^A$  are anharmonic contributions to the forces. The  $\langle \cdot \rangle$  indicates average value. The  $\mathbf{R}$  denotes the atomic positions. The larger  $\sigma^A(T)$  indicates the more anharmonicity in the material system and the lower thermal conductivity [62]. Figures 5(c) and 5(f) shows the Cu has the largest  $\sigma^A$  in the whole temperature region. Besides, the values of  $\sigma^A$  of Cu in CuInX<sub>2</sub>(X=Se, Te) are well

above the average value, which indicates the Cu contributes mostly to the anharmonicity. The largest contribution of Cu to anharmonicity is consistent with the projected DOS of Cu showing the obvious change with temperature as shown in Figs. 1(b), 1(c), 1(e), and 1(f). So the motion of Cu is very sensitive to the temperature and it leads to strong anharmonicity to make the phonon renormalization non-negligible for calculating the accurate lattice dynamic and thermal conductivity in CuInX<sub>2</sub>(X=Se, Te).

#### IV. CONCLUSION

Our results show that the strong phonon anharmonicity plays a critical role in explaining the significant deviation of  $\kappa_L \sim T^{-1}$  relation in CuInX<sub>2</sub>(X=Se, Te). It is demonstrated that the quasiharmonic approximation completely fails at high temperature in these two material systems. The optical phonon bands become obviously softened after considering the phonon anharmonicity, which leads to the small low energy phonon bandwidth and pseudo band gap. Compared with only using force constants at 300 K, the calculated thermal conductivity at high temperature decreases significantly (49% in CuInSe<sub>2</sub> at 750 K and 70% in CuInTe<sub>2</sub> at 850 K)

after using temperature dependent force constants. This dramatic decrease of thermal conductivity at high temperature is closely related to the temperature sensitive FC2 which induces enlarged phonon scattering phase space and brings enhanced scattering rate after considering the phonon anharmonicity. The temperature sensitive motion of Cu contributes mostly to the strong anharmonicity. Our results provide an understanding for the strong temperature dependent thermal conductivity and indicate the phonon engineering could be an effective way to modulate the thermal conductivity of Cu-based diamond-like chalcopyrite compounds.

## ACKNOWLEDGMENTS

The authors thank E. Fransson at Chalmers University of Technology for the helpful discussions. The work at Beijing Institute of Technology is supported by the National Key R&D Program of China (2021YFA1400300), Beijing Natural Science Foundation (Grant No. Z190011) and Graduate Technological Innovation Project of Beijing Institute of Technology (Grant No. 2022YCX001). Theoretical calculations were performed using resources of the Supercomputer Centre in Chongqing.

- 
- [1] G. Tan, L.-D. Zhao, and M. G. Kanatzidis, Rationally designing high-performance bulk thermoelectric materials, *Chem. Rev.* **116**, 12123 (2016).
- [2] J. He and T. M. Tritt, Advances in thermoelectric materials research: Looking back and moving forward, *Science* **357**, eaak9997 (2017).
- [3] M. A. Green and S. P. Bremner, Energy conversion approaches and materials for high-efficiency photovoltaics, *Nat. Mater.* **16**, 23 (2017).
- [4] J. Yang, X. Wen, H. Xia, R. Sheng, Q. Ma, J. Kim, P. Tapping, T. Harada, T. W. Kee, F. Huang, Y.-B. Cheng, M. Green, A. Ho-Baillie, S. Huang, S. Shrestha, R. Patterson, and G. Conibeer, Acoustic-optical phonon up-conversion and hot-phonon bottleneck in lead-halide perovskites, *Nat. Commun.* **8**, 14120 (2017).
- [5] N. P. Padture, M. Gell, and E. H. Jordan, Thermal barrier coatings for gas-turbine engine applications, *Science* **296**, 280 (2002).
- [6] G. J. Snyder and E. S. Toberer, Complex thermoelectric materials, *Nat. Mater.* **7**, 105 (2008).
- [7] E. Skoplaki and J. A. Palyvos, On the temperature dependence of photovoltaic module electrical performance: A review of efficiency/power correlations, *Solar Energy* **83**, 614 (2009).
- [8] G. Divitini, S. Cacovich, F. Matteocci, L. Ciná, A. Di Carlo, and C. Ducati, In situ observation of heat-induced degradation of perovskite solar cells, *Nat. Energy* **1**, 1 (2016).
- [9] R. Liu, L. Xi, H. Liu, X. Shi, W. Zhang, and L. Chen, Ternary compound CuInTe<sub>2</sub>: A promising thermoelectric material with diamond-like structure, *Chem. Commun.* **48**, 3818 (2012).
- [10] B. Wang, H. Xiang, T. Nakayama, J. Zhou, and B. Li, Theoretical investigation on thermoelectric properties of Cu-based chalcopyrite compounds, *Phys. Rev. B* **95**, 035201 (2017).
- [11] T. Plirdpring, K. Kurosaki, A. Kosuga, T. Day, S. Firdosy, V. Ravi, G. J. Snyder, A. Harnwungmoung, T. Sugahara, Y. Ohishi, H. Muta, and S. Yamanaka, Chalcopyrite CuGaTe<sub>2</sub>: A high-efficiency bulk thermoelectric material, *Adv. Mater.* **24**, 3622 (2012).
- [12] T. Feurer, R. Carron, G. Torres Sevilla, F. Fu, S. Pisoni, Y. E. Romanyuk, S. Buecheler, and A. N. Tiwari, Efficiency improvement of near-stoichiometric CuInSe<sub>2</sub> solar cells for application in tandem devices, *Adv. Energy Mater.* **9**, 1901428 (2019).
- [13] M. G. Panthani, V. Akhavan, B. Goodfellow, J. P. Schmidtke, L. Dunn, A. Dodabalapur, P. F. Barbara, and B. A. Korgel, Synthesis of CuInS<sub>2</sub>, CuInSe<sub>2</sub>, and Cu(In<sub>x</sub>Ga<sub>1-x</sub>)Se<sub>2</sub> (CIGS) Nanocrystal “Inks” for printable photovoltaics, *J. Am. Chem. Soc.* **130**, 16770 (2008).
- [14] T. Wada, CuInSe<sub>2</sub> and related I-III-VI<sub>2</sub> chalcopyrite compounds for photovoltaic application, *Jpn. J. Appl. Phys.* **60**, 080101 (2021).
- [15] S. Duan, W. Xue, H. Yao, X. Wang, C. Wang, S. Li, Z. Zhang, L. Yin, X. Bao, L. Huang, X. Wang, C. Chen, J. Sui, Y. Chen, J. Mao, F. Cao, Y. Wang, and Q. Zhang, Achieving high thermoelectric performance by NaSbTe<sub>2</sub> alloying in GeTe for simultaneous suppression of Ge vacancies and band tailoring, *Adv. Energy Mater.* **12**, 2103385 (2022).
- [16] S. Hao, V. P. Dravid, M. G. Kanatzidis, and C. Wolverton, Computational strategies for design and discovery of nanostructured thermoelectrics, *npj Comput. Mater.* **5**, 1 (2019).
- [17] C. Chen, Z. Feng, H. Yao, F. Cao, B.-H. Lei, Y. Wang, Y. Chen, D. J. Singh, and Q. Zhang, Intrinsic nanostructure induced ultralow thermal conductivity yields enhanced thermoelectric performance in zintl phase Eu<sub>2</sub>ZnSb<sub>2</sub>, *Nat. Commun.* **12**, 5718 (2021).
- [18] W. Li, J. Carrete, N. A. Katcho, and N. Mingo, ShengBTE: A solver of the boltzmann transport equation for phonons, *Comput. Phys. Commun.* **185**, 1747 (2014).
- [19] T. Tadano, Y. Gohda, and S. Tsuneyuki, Anharmonic force constants extracted from first-principles molecular dynamics: Applications to heat transfer simulations, *J. Phys.: Condens. Matter* **26**, 225402 (2014).
- [20] R. Hanus, R. Gurunathan, L. Lindsay, M. T. Agne, J. Shi, S. Graham, and G. Jeffrey Snyder, Thermal transport in defective and disordered materials, *Appl. Phys. Rev.* **8**, 031311 (2021).
- [21] J. Cai, J. Yang, G. Liu, H. Wang, F. Shi, X. Tan, Z. Ge, and J. Jiang, Ultralow thermal conductivity and improved ZT of CuInTe<sub>2</sub> by high-entropy structure design, *Mater. Today Phys.* **18**, 100394 (2021).
- [22] Y. Yan, X. Lu, G. Wang, and X. Zhou, zT=1.1 in CuInTe<sub>2</sub> solid solutions enabled by rational defect engineering, *ACS Appl. Energy Mater.* **3**, 2039 (2020).
- [23] A. Kosuga, K. Umekage, M. Matsuzawa, Y. Sakamoto, and I. Yamada, Room-temperature pressure-induced nanostructural CuInTe<sub>2</sub> thermoelectric material with low thermal conductivity, *Inorg. Chem.* **53**, 6844 (2014).
- [24] L. A. Makovetskaya, I. V. Bodnar, B. V. Korzun, and G. P. Yaroshevich, Thermal conductivity, thermoelectric power, and thermal expansion of CuInS<sub>2x</sub>Se<sub>2(1-x)</sub>, *Phys. Stat. Solidi A* **74**, K59 (1982).

- [25] Y. Li, J. Liu, X. Wang, and J. Hong, Anomalous Suppressed Thermal Conductivity in  $\text{CuInTe}_2$  under Pressure, *Appl. Phys. Lett.* **119**, 243901 (2021).
- [26] J. J. Plata, V. Posligua, A. M. Márquez, J. Fernandez Sanz, and R. Grau-Crespo, Charting the lattice thermal conductivities of I-III-VI<sub>2</sub> chalcopyrite semiconductors, *Chem. Mater.* **34**, 2833 (2022).
- [27] T. Tadano and S. Tsuneyuki, Quartic Anharmonicity of Rattlers and Its Effect on Lattice Thermal Conductivity of Clathrates from First Principles, *Phys. Rev. Lett.* **120**, 105901 (2018).
- [28] M. Simoncelli, N. Marzari, and F. Mauri, Unified theory of thermal transport in crystals and glasses, *Nat. Phys.* **15**, 809 (2019).
- [29] Z. Li, H. Xie, S. Hao, Y. Xia, X. Su, M. G. Kanatzidis, C. Wolverton, and X. Tang, Optical phonon dominated heat transport: A first-principles thermal conductivity study of  $\text{BaSnS}_2$ , *Phys. Rev. B* **104**, 245209 (2021).
- [30] Y. Xia, K. Pal, J. He, V. Ozolins, and C. Wolverton, Particlelike Phonon Propagation Dominates Ultralow Lattice Thermal Conductivity in Crystalline  $\text{Tl}_3\text{VSe}_4$ , *Phys. Rev. Lett.* **124**, 065901 (2020).
- [31] K. Pal, Y. Xia, and C. Wolverton, Microscopic mechanism of unusual lattice thermal transport in  $\text{TlInTe}_2$ , *npj Comput. Mater.* **7**, 1 (2021).
- [32] Y. Zhu, Y. Xia, Y. Wang, Y. Sheng, J. Yang, C. Fu, A. Li, T. Zhu, J. Luo, C. Wolverton, G. J. Snyder, J. Liu, and W. Zhang, Violation of the  $T^{-1}$  relationship in the lattice thermal conductivity of  $\text{Mg}_3\text{Sb}_2$  with locally asymmetric vibrations, *Research* **2020**, 4589786 (2020).
- [33] J. Klarbring, O. Hellman, I. A. Abrikosov, and S. I. Simak, Anharmonicity and Ultralow Thermal Conductivity in Lead-Free Halide Double Perovskites, *Phys. Rev. Lett.* **125**, 045701 (2020).
- [34] S. Mukhopadhyay, D. S. Parker, B. C. Sales, A. A. Puretzky, M. A. McGuire, and L. Lindsay, Two-channel model for ultralow thermal conductivity of crystalline  $\text{Tl}_3\text{VSe}_4$ , *Science* **360**, 1455 (2018).
- [35] T. Feng, L. Lindsay, and X. Ruan, Four-phonon scattering significantly reduces intrinsic thermal conductivity of solids, *Phys. Rev. B* **96**, 161201(R) (2017).
- [36] J. S. Kang, M. Li, H. Wu, H. Nguyen, and Y. Hu, Experimental observation of high thermal conductivity in boron arsenide, *Science* **361**, 575 (2018).
- [37] K. Chen, B. Song, N. K. Ravichandran, Q. Zheng, X. Chen, H. Lee, H. Sun, S. Li, G. A. G. U. Gamage, F. Tian, Z. Ding, Q. Song, A. Rai, H. Wu, P. Koirala, A. J. Schmidt, K. Watanabe, B. Lv, Z. Ren, L. Shi *et al.*, Ultrahigh thermal conductivity in isotope-enriched cubic boron nitride, *Science* **367**, 555 (2020).
- [38] R. Hanus, J. George, M. Wood, A. Bonkowski, Y. Cheng, D. L. Abernathy, M. E. Manley, G. Hautier, G. J. Snyder, and R. P. Hermann, Uncovering design principles for amorphous-like heat conduction using two-channel lattice dynamics, *Mater. Today Phys.* **18**, 100344 (2021).
- [39] H. Yu, L.-C. Chen, H.-J. Pang, P.-F. Qiu, Q. Peng, and X.-J. Chen, Temperature-dependent phonon anharmonicity and thermal transport in  $\text{CuInTe}_2$ , *Phys. Rev. B* **105**, 245204 (2022).
- [40] H. Tanino, T. Maeda, H. Fujikake, H. Nakanishi, S. Endo, and T. Irie, Raman spectra of  $\text{CuInSe}_2$ , *Phys. Rev. B* **45**, 13323 (1992).
- [41] C. Rincón and F. J. Ramírez, Lattice vibrations of  $\text{CuInSe}_2$  and  $\text{CuGaSe}_2$  by raman microspectrometry, *J. Appl. Phys.* **72**, 4321 (1992).
- [42] C. Rincón, S. M. Wasim, G. Marín, J. R. Huntzinger, A. Zwick, and J. Galibert, Raman spectra of the chalcopyrite compound  $\text{CuInTe}_2$ , *J. Appl. Phys.* **85**, 3925 (1999).
- [43] G. Sun, J. Kürti, P. Rajczy, M. Kertesz, J. Hafner, and G. Kresse, Performance of the vienna *Ab Initio* simulation package (VASP) in chemical applications, *J. Mol. Struct. (THEOCHEM)* **624**, 37 (2003).
- [44] See Supplemental Material at <http://link.aps.org/supplemental/10.1103/PhysRevB.106.094317> for three notes (Comparison between LDA and GGA; Lattice constant used in temperature dependent calculation and Convergence tests), six figures (Convergence of cutoff radii second order force constants for phonon renormalization, Convergence of cutoff radii of third order force constants, Convergence test of q mesh for calculating thermal conductivity; Convergence test of number of configurations for extracting force constant; Temperature dependent group velocity of  $\text{CuInX}_2$  along  $\Gamma - Y$  direction and Temperature dependent phonon dispersion of  $\text{CuInX}_2$  with Grüneisen parameter) and four tables (Comparison of the calculated lattice constants from LDA and GGA with experiment results; The thermal expansion coefficient; The lattice constant of  $\text{CuInX}_2$  for TDEP calculation and Comparison of the calculated frequencies  $\omega_{\text{cal}}$  at  $\Gamma$  with the Raman experimental  $\omega_{300\text{K}}$ ).
- [45] Y. Cao, X. Su, F. Meng, T. P. Bailey, J. Zhao, H. Xie, J. He, C. Uher, and X. Tang, Origin of the distinct thermoelectric transport properties of chalcopyrite  $\text{ABTe}_2$  ( $A=\text{Cu, Ag}$ ;  $B=\text{Ga, In}$ ), *Adv. Funct. Mater.* **30**, 2005861 (2020).
- [46] H. J. Monkhorst and J. D. Pack, Special points for brillouin-zone integrations, *Phys. Rev. B* **13**, 5188 (1976).
- [47] W. Paszkowicz, R. Minikayev, P. Piszora, D. Trots, M. Knapp, T. Wojciechowski, and R. Bacewicz, Thermal expansion of  $\text{CuInSe}_2$  in the 11–1073 K range: An X-ray diffraction study, *Appl. Phys. A* **116**, 767 (2014).
- [48] I. V. Bodnar and N. S. Orlova, Lattice thermal expansion in  $\text{CuGaTe}_2$  and  $\text{CuInTe}_2$  compounds over the temperature range 80 to 650 K from X-ray diffraction data, *Cryst. Res. Technol.* **21**, 1091 (1986).
- [49] A. Togo and I. Tanaka, First-principles phonon calculations in materials science, *Scr. Mater.* **108**, 1 (2015).
- [50] O. Hellman, I. A. Abrikosov, and S. I. Simak, Lattice dynamics of anharmonic solids from first principles, *Phys. Rev. B* **84**, 180301(R) (2011).
- [51] O. Hellman, P. Steneteg, I. A. Abrikosov, and S. I. Simak, Temperature dependent effective potential method for accurate free energy calculations of solids, *Phys. Rev. B* **87**, 104111 (2013).
- [52] O. Hellman and I. A. Abrikosov, Temperature-dependent effective third-order interatomic force constants from first principles, *Phys. Rev. B* **88**, 144301 (2013).
- [53] J. H. Lloyd-Williams and B. Monserrat, Lattice dynamics and electron-phonon coupling calculations using nondiagonal supercells, *Phys. Rev. B* **92**, 184301 (2015).
- [54] F. Eriksson, E. Fransson, and P. Erhart, The hiphive package for the extraction of high-order force constants by machine learning, *Adv. Theory Simul.* **2**, 1800184 (2019).
- [55] J. Brorsson, A. Hashemi, Z. Fan, E. Fransson, F. Eriksson, T. Ala-Nissila, A. V. Krasheninnikov, H.-P. Komsa, and P. Erhart,



- Efficient calculation of the lattice thermal conductivity by atomistic simulations with *Ab Initio* accuracy, *Adv. Theory Simul.* **5**, 2100217 (2022).
- [56] R. Liu, Y. Qin, N. Cheng, J. Zhang, X. Shi, Y. Grin, and L. Chen, Thermoelectric performance of  $\text{Cu}_{1-x-\delta}\text{Ag}_x\text{InTe}_2$  diamond-like materials with a pseudocubic crystal structure, *Inorg. Chem. Front.* **3**, 1167 (2016).
- [57] J. Yao, N. J. Takas, M. L. Schliefert, D. S. Paprocki, P. E. R. Blanchard, H. Gou, A. Mar, C. L. Exstrom, S. A. Darveau, P. F. P. Poudeu, and J. A. Aitken, Thermoelectric properties of *P*-Type  $\text{CuInSe}_2$  chalcopyrites enhanced by introduction of manganese, *Phys. Rev. B* **84**, 075203 (2011).
- [58] C. W. Li, J. Hong, A. F. May, D. Bansal, S. Chi, T. Hong, G. Ehlers, and O. Delaire, Orbitaly driven giant phonon anharmonicity in  $\text{SnSe}$ , *Nat. Phys.* **11**, 1063 (2015).
- [59] L. Lindsay and D. A. Broido, Three-phonon phase space and lattice thermal conductivity in semiconductors, *J. Phys.: Condens. Matter* **20**, 165209 (2008).
- [60] K. Yuan, X. Zhang, D. Tang, and M. Hu, Anomalous pressure effect on the thermal conductivity of  $\text{ZnO}$ ,  $\text{GaN}$ , and  $\text{AlN}$  from first-principles calculations, *Phys. Rev. B* **98**, 144303 (2018).
- [61] J. Hempelmann, P. C. Müller, P. M. Konze, R. P. Stoffel, S. Steinberg, and R. Dronskowski, Long-range forces in rock-salt-type tellurides and how they mirror the underlying chemical bonding, *Adv. Mater.* **33**, 2100163 (2021).
- [62] F. Knoop, T. A. R. Purcell, M. Scheffler, and C. Carbogno, Anharmonicity measure for materials, *Phys. Rev. Mater.* **4**, 083809 (2020).